Applied Catalysis B: Environmental 239 (2018) 27–35

Contents lists available at ScienceDirect

Applied Catalysis B: Environmental

journal homepage: www.elsevier.com/locate/apcatb

Metal-oxide interaction enhanced CO_2 activation in methanation over ceria supported nickel nanocrystallites

Maoshuai Li[a,*], Houari Amari[b], André C. van Veen[a,*]

[a] School of Engineering, The University of Warwick, Coventry CV4 7AL, United Kingdom
[b] Department of Physics, The University of Warwick, Coventry CV4 7AL, United Kingdom

ARTICLE INFO

Keywords:
CO_2 methanation
Metal-oxide interaction
Ni/CeO_2
Decoration/encapsulation
TAP

ABSTRACT

The role of metal-support interaction in determining CO_2 activation and conversion for methane production was examined over (CeO_2, TiO_2 and SiO_2) supported Ni nanoparticles. Hexagonal Ni nanocrystallites on CeO_2 with strong metal-oxide interaction selectively produced CH_4 at (up to forty-fold) higher turnover frequencies (TOFs) than that recorded over (TiO_2 and SiO_2) supported Ni nanoparticles. A stronger adsorption of CO_2 and H_2 was identified for Ni/CeO_2 using temporal analysis of products (TAP). Decoration/encapsulation of Ni nanoparticles by a thin layer of reduced ceria can decrease the catalytic capacity for CO_2 activation/conversion. An initial loss of activity in the long-term stability evaluation over Ni/CeO_2 can be linked to a reconstruction of hexagonal Ni nanocrystallites to quasi-spherical particles.

1. Introduction

Metal-oxide interface, a phase boundary formed by strong bonding interaction between metal and oxide crystallites, is a region of special catalytic activity in heterogeneous supported metal catalysis [1–4]. Experimental (STM, XPS, UPS, EELS and STEM) and theoretical (DFT) studies have demonstrated a number of interfacial effect including charge transfer, cluster stabilisation and decoration/encapsulation of metal nanoparticles on oxide supported metal catalysis [5–10]. Notably decoration/encapsulation of metal nanoparticles by reducible oxide layers, as a typical case of strong metal-support interaction (SMSI), has been identified as a means of tuning metal-catalyst reactivity [10–12]. CO_2 hydrogenation rate can be controlled in methanol production over CeO_x/Cu (111) via adjusting coverage of Cu (111) surface by depositing CeO_x layer, where complete coverage of Cu (111) blocked the metal surface and rendered the catalyst inactive [12]. Moreover, SMSI-induced metal encapsulation has been found to control reaction selectivity via modification of the encapsulation layers. Matsubu et al. [13] have demonstrated an atom-scale porous support oxide layer on Rh nanoparticles allowed small molecules for an access to the metal surface and induced a selectivity switch from CH_4 on bare Rh particles to CO production in CO_2 reduction.

The existing studies associated with metal-oxide interaction in supported metal catalysis has been focusing on decoration of noble metals (Rh [14–16], Ru [17,18], Pt [19–21], Au [22–24]) with less attention on non-noble metals (e.g., Ni and Co). Ceria is an example of an active oxide that is widely used as support due to surface deficiencies in heterogeneous catalysis [25]. Metal nanoparticle is facile to form interaction with ceria [4]. Nickel is a typical transition metal catalyst. In this study, we consider (non-noble) metal-oxide interface by high temperature (673–973 K) treatment of Ni impregnated on CeO_2 in H_2 and the effect of tuning metal-oxide interaction on the morphology of the supported Ni nanocrystallites. The methanation of CO_2 for methane production is of great significance in terms of storage of excess hydrogen derived from biomass, reduction of CO_2 emission and production of natural gas [26]. CO_2 methanation has been studied over Ni catalysts supported on oxides [27–29]. Activation of CO_2 for cleavage of the C═O bond is crucial in determining the methanation efficiency [30]. However, the catalytic species for CO_2 activation are less than well understood. In this study, we examine the role of metal-support interaction in determining CO_2 adsorption/activation/conversion in methanation over Ni nanoparticles on reducible (CeO_2 and TiO_2) and non-reducible (SiO_2) supports. Ni sintering and carbon formation was considered for the catalyst stability.

2. Experimental

2.1. Materials and catalyst preparation

Commercial CeO_2 (Sigma-Aldrich), TiO_2 (P25, Sigma-Aldrich),

* Corresponding authors.
E-mail addresses: maoshuaili@sina.com (M. Li), Andre.vanVeen@warwick.ac.uk (A.C. van Veen).

https://doi.org/10.1016/j.apcatb.2018.07.074
Received 11 April 2018; Received in revised form 21 July 2018; Accepted 27 July 2018
Available online 29 July 2018
0926-3373/ Crown Copyright © 2018 Published by Elsevier B.V. All rights reserved.

fused SiO_2 (Sigma-Aldrich) and NiO (Alfa Aesar) were used as received. The supported (5 wt%) Ni catalysts were prepared by wet-impregnation. The supports (5 g) were added to aqueous solution of $Ni(NO_3)_2$ (Alfa Aesar, 98%, 9×10^{-2} M, 50 cm^3) and stirred (500 rpm) at room temperature overnight. The solid was obtained by evaporation and dried in air at 393 K overnight. The resultant samples were sieved (ATM fine test sieves) to mean particle diameter = 75 μm, activated at 10 K min^{-1} to 723–973 K in 10 $cm^3\,min^{-1}$ H_2, cooled to ambient temperature and passivated in 1% v/v O_2/N_2 for 1 h for *ex situ* characterisation (including N_2 physisorption, XRD, UV Raman and TEM).

2.2. Catalyst characterisation

Nitrogen physisorption was performed on the Micromeritics ASAP 2020 system and total specific surface area (SSA) calculated using the standard BET method. Prior to analysis, samples were vacuumed and outgassed at 573 K for 1 h. Temperature programmed reduction (TPR) was conducted in a quartz tube cell. The sample was heated in 84 $cm^3\,min^{-1}$ 5% v/v H_2/Ar at 10 K min^{-1} to 723 K and held for 1 h. Hydrogen consumption was monitored by a thermal conductivity detector (TCD). X-ray diffractograms (XRD) were recorded on a Panalytical Empyrean X-ray diffractometer using Co or Cu Kα radiation. Samples were scanned at 0.01° $step^{-1}$ over the range $20° \leq 2\theta \leq 80°$ at ambient temperature and the diffractograms identified against the JCPDS-ICDD reference standards. Metal particle morphology (size and shape) was examined by high resolution transmission electron microscopy (HRTEM, JEOL 2100 LaB6), employing Gatan Digital Micrograph for data acquisition/manipulation. Samples for analysis were prepared by dispersion in ethanol and deposited on a holey carbon/Cu grid. XPS measurements of the reduced samples were performed on a Kratos Axis Ultra DLD spectrometer using a monochromated Al kα X-ray source. The samples were attached to electrically-conductive carbon tape and mounted on to a sample bar. The measurements were conducted at room temperature and at a take-off angle of 90° with respect to the surface parallel. The spectrometer work function and binding energy scale were calibrated using the Fermi edge and $3d_{5/2}$ peak recorded from a polycrystalline Ag sample prior to the commencement of the experiments. To avoid the possibility of differential charging, the samples were allowed to float and surface charging negated using a charge neutraliser. Ni $2p_{3/2}$, Ce 3d, Ti 2p and Si 2p spectra were collected. Characteristic Ni $2p_{3/2}$ binding energy (BE) for metallic Ni is 852.5 ev and 856.3 ev; for NiO is 853.7 ev, 855.4 ev and 861.0 ev [31]. The BE scale was calibrated by positioning the sp3 (C-C/C-H) component of the C 1 s region at 285.0 ev. The data were analysed in CasaXPS, using Shirley backgrounds and mixed Gaussian-Lorentzian (Voigt) lineshapes and asymmetry parameters where appropriate. UV Raman spectra was recorded on a Renishaw inVia Raman spectrometer equipped with HeCd laser at an excitation wavelength (λ) = 325 nm using ×5 objective and grating of 3600 lines mm^{-1}. Thermogravimetric-derivative thermogravimetric analysis (TGA-DTG) was conducted on a simultaneous thermal analyser (NETZSCH STA449) by monitoring temporal mass with temperature. The samples (ca. 30 mg) were heated in 50 $cm^3\,min^{-1}$ air to 973 K (at 10 K min^{-1}).

2.3. Catalyst testing

The methanation reaction was carried out at atmospheric pressure and 473–523 K in situ after activation (673–973 K) in a continuous flow fixed bed tubular reactor (10 mm i.d.). Reactions were conducted under operating conditions that ensured negligible mass/heat transport limitations. Isothermal conditions (± 1 K) were ensured by diluting the catalyst bed with ground glass (75 μm); the ground glass was mixed thoroughly with catalyst before loading into the reactor. Reaction temperature was continuously monitored by a thermocouple inserted in the catalyst bed. CO_2 (BOC, 99.99%), H_2 (BOC, 99.99%), N_2 (BOC, 99.99%) and Ar (BOC, 99.99%) was introduced to reactor by Brooks mass flow controller (SLA5800 series) at GHSV = 1.6×10^4–$6.6 \times 10^4\,h^{-1}$. Inlet H_2 to CO_2 feeding rate was fixed at 4:1. 0.02-0.08 g catalyst was used in the reaction. The molar Ni to inlet CO_2 feeding rate (n/F_{CO_2}) was in the range 6.5×10^{-3}–2.6×10^{-2} h. The reactor effluent was analysed using online gas chromatography (Shimadzu 2014) equipped with a 0.5 cm^3 sampling loop, thermal conductive detector (TCD) and flame ionization detector (FID), employing serial Hayesep Q (3.0 m × 2.1 mm i.d.) and Molecular Sieve 5 A packed columns (2.0 m × 2.1 mm i.d.). Data acquisition and manipulation were performed using GCsolution Lite (Version 2.4) chromatography data system. CO_2 fractional conversion (X_{CO_2}) is defined by:

$$X_{CO2} = \frac{[CO_2]_{in} - [CO_2]_{out}}{[CO_2]_{in}} \quad (1)$$

and product 'j' selectivity (*S*j) is defined by:

$$S_j(\%) = \frac{[product]_{j,out}}{[CO_2]_{in} - [CO_2]_{out}} \times 100 \quad (2)$$

CO_2 consumption rate (R_{CO_2}, h^{-1}) was obtained from:

$$R_{CO2} = \frac{[CO_2]_{in} \times X_{CO2}}{n} \quad (3)$$

where subscripts "in" and "out" refer to inlet and outlet gas streams. Turnover frequency (TOF, rate per active site) was calculated using:

$$TOF\,(h^{-1}) = \frac{R_{CO2}}{D} \quad (4)$$

D is the Ni dispersion (surface metal per total metal atoms) obtained from:

$$D = \frac{(6/d \times \rho_{Ni}) \times M_{Ni}}{A_{Ni} \times N_{Avogadro}} \quad (5)$$

where d (mean size) is obtained from TEM measurements, ρ_{Ni}: the Ni density, M_{Ni}: Ni atom mass, A_{Ni}: Ni atom surface area and N: Avogadro number. In blank tests, passage of CO_2 in a stream of H_2 through the empty reactor or over support alone did not result in any detectable conversion. Repeated reactions delivered data reproducibility and carbon balance within 7%.

CO_2 and H_2 pulse experiments using temporal analysis of products (TAP) were carried out at 523 K under high-vacuum conditions after in situ activation (50% v/v H_2/Ar, 723 K) in a temporal-analysis of products setup as described elsewhere [32]. The catalyst (20 mg) was packed between two layers of quartz wool in a quartz tube reactor. Reaction temperature was monitored by a thermocouple inserted in the catalyst bed. Approximately 2×10^{14} molecules of 50% v/v CO_2/Ar and 50% v/v H_2/Ar were pulsed to the catalyst bed by high-speed pulsed valves. The reactor effluent was detected with millisecond time resolution by the quadrupole mass spectrometer. Ar was monitored at m/e = 40, CO_2 at m/e = 44, H_2 at m/e = 2, CO at m/e = 28, CH_4 at m/e = 16 and H_2O at m/e = 18.

3. Results and discussion

3.1. Catalyst characterisation

The physicochemical characteristics of Ni/CeO_2, Ni/TiO_2 and Ni/SiO_2 (activated at 723 K) are given in Table 1. The supported Ni catalysts exhibited SSA (8-53 $m^2\,g^{-1}$) that is consistent with that reported in the literature [33–35]. TPR profiles generated for Ni/CeO_2, Ni/TiO_2 and Ni/SiO_2 can be compared in Fig. 1. Reduction of Ni/CeO_2 presented two H_2 consumption signals with associated temperature maxima (T_{max}) at 547 K and 639 K, corresponding to reduction of Ni^{2+} species that was in weaker and stronger interaction with support, respectively [36,37]. Hydrogen consumed (1.1 $mol_{H_2}{}^{-1}\,mol_{Ni}{}^{-1}$) during TPR of Ni/CeO_2 exceeded that (1.0 $mol_{H_2}{}^{-1}\,mol_{Ni}{}^{-1}$) required for NiO → Ni,

Table 1
SSA, temperature maximum (T_{max}) during TPR, mean Ni particle size (d) and Ni dispersion (D) from TEM analysis.

	Ni/CeO_2	Ni/TiO_2	Ni/SiO_2
SSA ($m^2\,g^{-1}$)	11	53	8
TPR T_{max} (K)	547, 639	718	652
d (nm)	8.7	9.4	5.3
D (%)	11.6	10.8	19.1

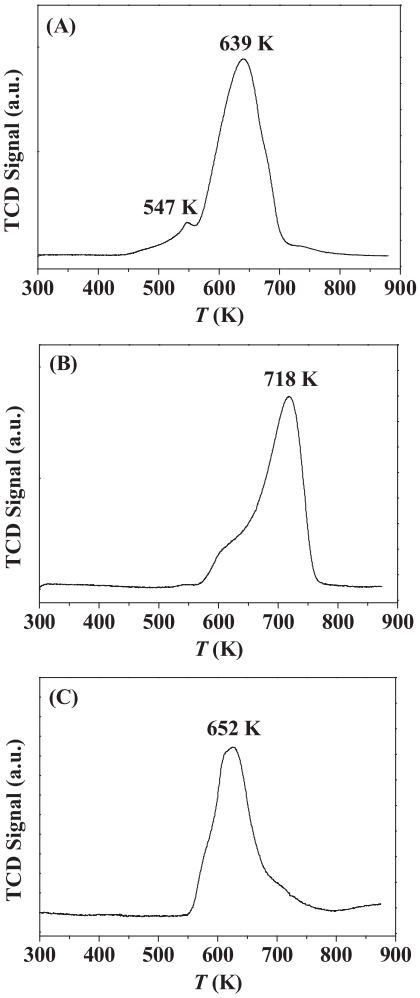

Fig. 1. Temperature programmed reduction (TPR) profiles for **(A)** Ni/CeO_2, **(B)** Ni/TiO_2 and **(C)** Ni/SiO_2.

suggesting partial support reduction ($Ce^{4+} \rightarrow Ce^{3+}$). The profile of Ni/TiO_2 exhibited a principle reduction peak at T_{max} = 718 K, where H_2 consumption matched that for Ni^{2+} reduction to Ni^0. TPR profile of Ni/SiO_2 showed a hydrogen consumption peak at 652 K, which was a result of NiO reduction [38]. Structure analysis by XRD (using Co radiation) generated diffraction patterns are shown in Fig. 2. Diffraction signals at 2θ = 52.1° and 61.0° corresponded to Ni (111) and (200) planes. There was no detectable signal due to NiO. XRD pattern of Ni/CeO_2 exhibited peaks at 2θ = 33.4°, 38.7°, 55.9°, 66.6° and 70.0° corresponding to cubic CeO_2 (111), (200), (220), (311) and (222). Analysis of Ni/TiO_2 revealed a mixture of rutile and anatase phases. The pattern of Ni/SiO_2 was characterised by diffraction peaks of fused SiO_2. Analysis by XPS provides information on surface composition and the chemical/electronic state of supported metal catalyst. Spectra over the Ni $2p_{3/2}$ (AI–CI), Ce 3d **(AII)**, Ti 2p **(BII)** and Si 2p **(CII)** BE regions are shown in Fig. 3. Ni $2p_{3/2}$ spectrum of the supported Ni catalysts exhibited

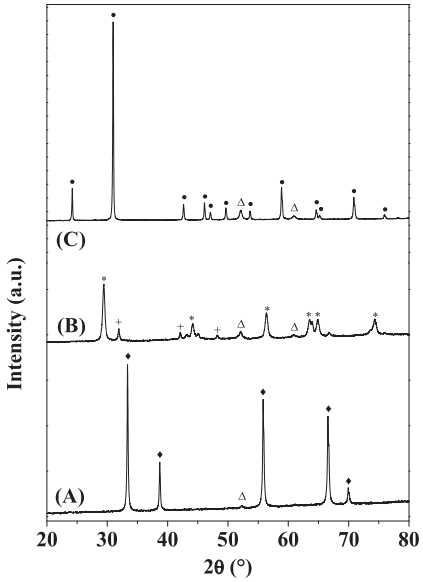

Fig. 2. XRD patterns for **(A)** Ni/CeO_2, **(B)** Ni/TiO_2 and **(C)** Ni/SiO_2 (Δ: Ni; ♦: CeO_2; *: anatase; +: rutile and ●: SiO_2).

common signals at 852.5 ± 0.2 ev, consistent with the reference metallic Ni (852.4–852.6 ev) [39]. Multi-split peaks at 853.6–853.8 ev, 855.6–855.9 ev and 861.0–861.2 ev match the characteristic Ni $2p_{3/2}$ BE of NiO (core level: 853.7 ev, 855.7 ev; satellite: 861.0 ev) [31,40]. The formation of NiO resulted from oxidation of metallic Ni when exposed to air [39]. Ni $2p_{3/2}$ spectrum of Ni/CeO_2 (Fig. 3**(AI)**) presented an additional core level peak at 856.9 ev with a satellite peak at 861.7 ev, which was a contribution of Ni^{2+} species that was bonded with ceria (Ni-O-Ce) at the interface. Biesinger et al. [41] have attributed Ni $2p_{3/2}$ signals at 856.5 ev and 861.3 ev to Ni^{2+} in $NiCrO_4$. The spectrum of Ce 3d **(AII)** showed up to ten signal components due to various final state electron configurations [42]. The peaks (denoted ν, ν_0, ν', ν" and ν"') were linked to Ce $3d_{5/2}$; while the signals (μ, μ_0, μ', μ" and μ"') corresponded to Ce $3d_{3/2}$. Ce^{4+} species generated peaks μ"' and ν"', μ" and ν", μ and ν due to $Ce3d^94f^0O2p^6$, $Ce3d^94f^1O2p^5$ and $Ce3d^94f^2O2p^4$ final state, respectively [43]. Ce^{3+} component was associated with the signals μ' and ν' corresponding to $Ce3d^94f^1O2p^6$ state, μ_0 and ν_0 resulting from $Ce3d^94f^2O2p^5$ state [43]. The ratio of $Ce^{3+}/(Ce^{3+} + Ce^{4+})$ was estimated to be 0.2, suggesting significant reduction of ceria surface ($Ce^{4+} \rightarrow Ce^{3+}$) with formation of oxygen vacancies. There was evidence showing thermal treatment of ceria in H_2 generated oxygen vacancies by loss of lattice oxygen [44]. Supported metal phase can facilitate generation of Ce^{3+} defects and surface oxygen vacancies due to spillover hydrogen [45]. The spectrum of Ti 2p **(BII)** showed Ti $2p_{3/2}$ and Ti $2p_{1/2}$ peak at 458.8 ev and 464.5 ev, which was associated with Ti^{4+} in TiO_2 [46]. There was no detectable signal due to surface Ti^{3+} species. Spectra **(CII)** of Ni/SiO_2 over the Si 2p BE region exhibited a signal at 104.6 ev due to SiO_2. UV Raman spectra is an effective characterisation means to detect deficient sites in ceria [47]. Activated CeO_2 and Ni/CeO_2 was subjected to UV Raman measurement with spectrum shown in Fig. 4. The Raman shift at 470 cm^{-1}, 590 cm^{-1} and 1171 cm^{-1} corresponded to F_{2g} symmetry mode, defect-induced mode (D band) and second order longitude optical mode (2LO), respectively [48]. The D band was associated with oxygen vacancies [49]. There was no significant peak associated with F2g and D band in the spectra of CeO_2, which may be below detection limit. The D band signal was recorded upon addition of Ni to CeO_2. The intensity ratio of D band to F2g band was ca. 0.98, larger than the values (ca. 0.41) reported in the literature [49], suggesting relatively higher density of oxygen vacancies on Ni/CeO_2. This can be linked to a contribution of hydrogen spillover from Ni particles to support facilitated ceria reduction ($Ce^{4+} \rightarrow Ce^{3+}$)

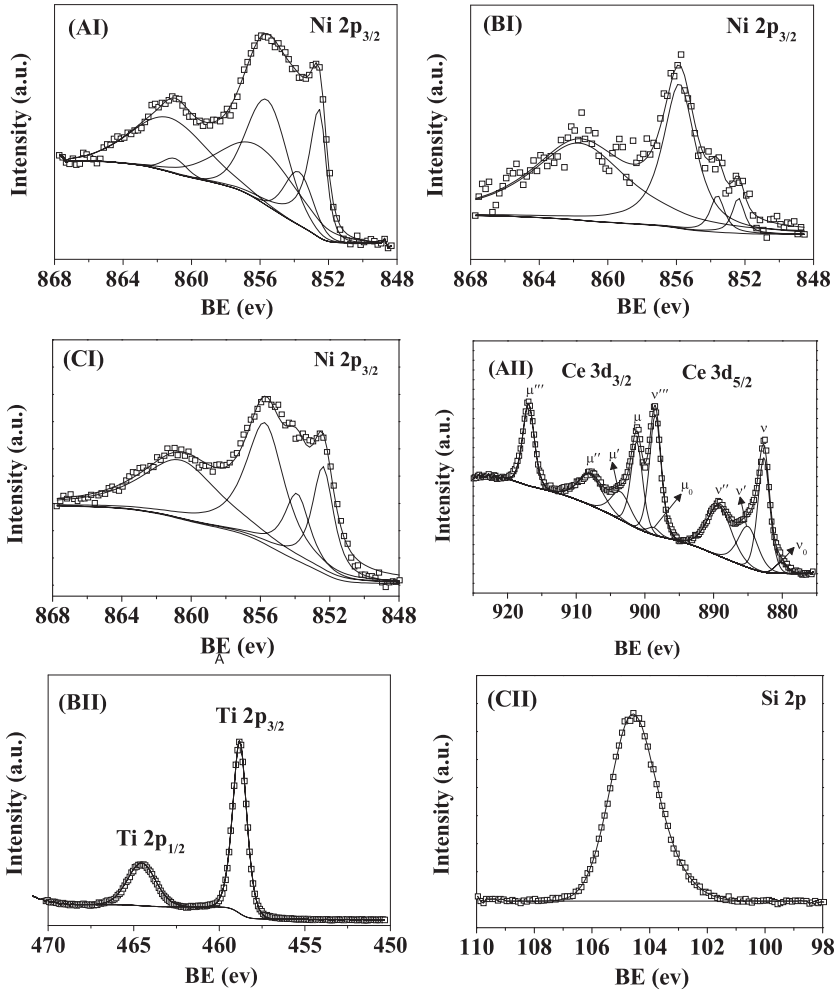

Fig. 3. XPS profile of **(I)** Ni $2p_{3/2}$ for **(A)** Ni/CeO_2, **(B)** Ni/TiO_2 and **(C)** Ni/SiO_2; and spectra of **(AII)** Ce 3d, **(BII)** Ti 2p and **(CII)** Si 2p.

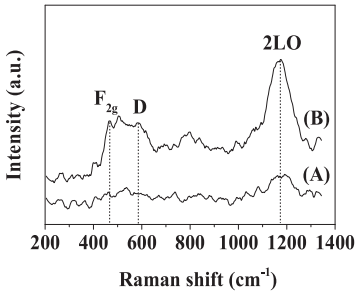

Fig. 4. UV Raman spectra of activated **(A)** CeO_2 and **(B)** Ni/CeO_2.

with greater oxygen vacancies formation.

Nickel particle morphology and metal-support interaction for the supported Ni catalysts (activated at 723 K) was evaluated by TEM. HRTEM image of Ni/CeO_2 (Fig. 5A) presented hexagonal Ni nanoparticles (3–14 nm, mean = 8.7 nm) with perimeter in the range of 10–40 nm (**Fig. S1A**). Atomic columns for Ni and Ce were clearly observed. Lattice fringe distance of Ni and CeO_2 were 0.2 nm and 0.31 nm, corresponding to Ni (111) and CeO_2 (111), respectively. We can note a few layers of the Ni surface were deficient, notably the left part of the Ni particle in the framed area, leading to exposure of ceria surface. Ni atoms were arranged in disorder with no clear atomic column due to surface dislocation, and surface defects (e.g., corners and holes) were formed on the Ni nanocrystallites (on the right side of the frame). Ni^{2+} cations can penetrate into the lattices of CeO_2 (110) and/or (111) facet by locating in vacant sites [49]. This incorporation resulted in formation of strong interaction between Ni and CeO_2 following high temperature reduction in H_2. In contrast to Ni/CeO_2, Ni/TiO_2 exhibited quasi-spherical Ni nanoparticles **(B)**. The Ni particle size distribution was in the 5–13 nm range with a similar mean (9.4 nm) to that of Ni/CeO_2 (**Fig. S1B**). The lattice spacing (0.33 nm) is consistent with TiO_2 (110) facet. An interphase boundary (dashed frame) between Ni and TiO_2 (110) was observed on Ni/TiO_2. Ni/SiO_2 **(C)** showed an appreciably wider size range of Ni particles (1–40 nm) with a mean size of 5.3 nm. No significant strong metal-support interaction was observed over Ni/SiO_2. This is consistent with that metal nanoparticles on reducible oxide support is more facile to generate strong metal-oxide interaction than non-reducible support [13].

3.2. Catalytic response: effect of metal-oxide interface

Turnover frequency of CO_2 (TOF_{CO_2}) and CH_4 selectivity with variation of temperature (473–523 K) in CO_2 methanation is presented in Fig. 6. Reaction (523 K) over Ni/CeO_2 delivered appreciably (up to forty-fold) higher TOF than TiO_2 and SiO_2 supported Ni catalysts. This value (271 h^{-1}) was appreciably higher than that reported over Ni nanoparticles in metal-organic framework MIL-101 (< 2 h^{-1}) [50], TiO_2 supported Pd (144 h^{-1}) and Pt (252 h^{-1}) [51] under similar conditions (523 K). It should be noted that there was no detectable conversion over Ni/SiO_2 at T ≤ 473 K. CeO_2 and TiO_2 supported Ni were fully selective to CH_4 in the temperature range (473–523 K). Reaction over Ni/SiO_2 (498 K) generated CH_4 as the sole product with CO

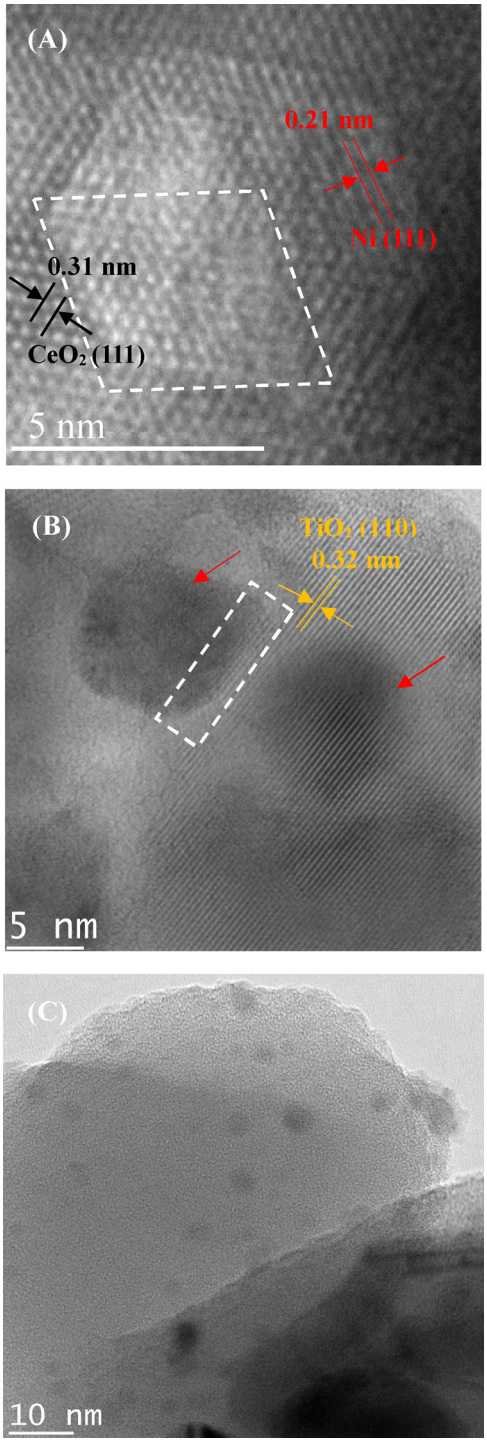

Fig. 5. Representative HRTEM images for **(A)** Ni/CeO_2, **(B)** Ni/TiO_2 and **(C)** Ni/SiO_2.

formation at elevated temperature (523 K). Metal particle size is a critical parameter in determining hydrogenation activity, where smaller metal particles generally facilitate hydrogenation [52]. In this study, Ni/CeO_2 exhibited appreciably higher TOFs than that recorded over Ni/TiO_2 that bears similar Ni particle size and the values for Ni/SiO_2 that shows smaller Ni particles (Table 1). This suggests Ni particle morphology, support and/or metal-support interface effect, rather than Ni particle sizes, determine the hydrogenation of CO_2 to CH_4. The catalytic response of the physical mixtures of Ni + CeO_2 and Ni/CeO_2 + CeO_2 was examined under the reaction conditions where the Ni content in the

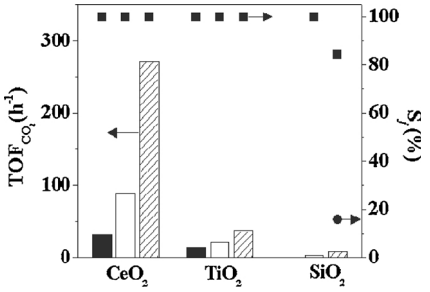

Fig. 6. Turnover frequency of CO_2 (TOF_{CO_2}) and product selectivity (Sj, ■: CH_4; ●: CO) as a function of temperature (solid bar: 473 K, open bar: 498 K, hatched bar: 523 K) in CO_2 methanation over the supported Ni catalysts. Reaction condition: T_{reduce} = 723 K, $n/F_{CO_2} = 6.5 \times 10^{-3}$–$2.6 \times 10^{-2}$ h, GHSV = 1.6×10^4–$6.6 \times 10^4\ h^{-1}$.

Table 2
CO_2 consumption rate (R_{CO_2}) in CO_2 methanation over Ni/CeO_2, physical mixture of Ni with CeO_2 and physical mixture of Ni/CeO_2 with CeO_2. Reaction condition: T_{react} = 523 K, T_{reduce} = 723 K, $n/F_{CO_2} = 6.5 \times 10^{-3}$ h, GHSV = $6.6 \times 10^4\ h^{-1}$.

Catalyst	Ni/CeO_2	Ni + CeO_2	Ni/CeO_2 + CeO_2
R_{CO_2} (h^{-1})	31.5	–	29.5

catalyst was kept constant and Ni/CeO_2 : CeO_2 = 1:1 (based on weight). There was no detectable conversion over the physical mixture of Ni + CeO_2. This suggests physical contact of Ni particles with CeO_2 has no catalytic activity for CO_2 and/or H_2 activation. Reaction over Ni/CeO_2 + CeO_2 mixture delivered exclusive selectivity to CH_4 at a CO_2 consumption rate similar to that recorded over Ni/CeO_2 (Table 2). This suggests incorporation of support as a physical mixture with Ni/CeO_2 does not dramatically influence the overall catalytic activity, which is controlled by Ni/CeO_2.

The interaction of CO_2 and H_2 with (CeO_2, TiO_2 and SiO_2) supported Ni catalysts was examined in pulse reactions using temporal analysis of products. The response signals as a flux of the reactor effluent versus time are presented in Fig. 7. The amount of CO_2 leaving the reactor followed an increasing order: Ni/CeO_2 < Ni/TiO_2 < < Ni/SiO_2 < CeO_2 < blank **(I)**, suggesting a stronger adsorption of CO_2 with Ni/CeO_2. A small decrease in CO_2 response over ceria relative to that in the blank testing demonstrates the support alone was not crucial in determining the adsorption of CO_2. There was no significant difference in H_2 uptake among the Ni catalysts **(II)**. This implies the catalyst capacity for adsorption/activation of CO_2 determines the methanation activity. CO was produced over Ni/TiO_2 and Ni/SiO_2. There was no detectable CH_4 formation for all the catalysts. We can note the amount of CO generation matched CO_2 consumption in the reaction over Ni/SiO_2 **(III)**, indicating complete reduction of CO_2 to CO. The reaction over Ni/TiO_2 generated a smaller amount of CO (relative to Ni/SiO_2), appreciably lower than the CO_2 consumption. No CO was detected over Ni/CeO_2, suggesting Ni/CeO_2 facilitated conversion of CO_2 to a carbonaceous (e.g., formate) intermediate that was adsorbed on the catalyst surface without further reaction with hydrogen to form methane under the pulse reaction condition where the feeding ratio CO_2 : H_2 = 1:1 was lower than the stoichiometry. Metal-oxide interface is a special region of active sites [3]. Metal nanoparticle morphology determines the exposed active facets [53]. We consider a synergistic cooperation of hexagonal Ni nanocrystallites with metal-oxide interface enhanced the CO_2 methanation rate over Ni/CeO_2. CO_2 is preferentially adsorbed/activated at the interface between Ni and CeO_2. Hexagonal Ni nanocrystallites facilitate H_2 activation/dissociation to atomic hydrogen that participates in CO_2 hydrogenation to CH_4.

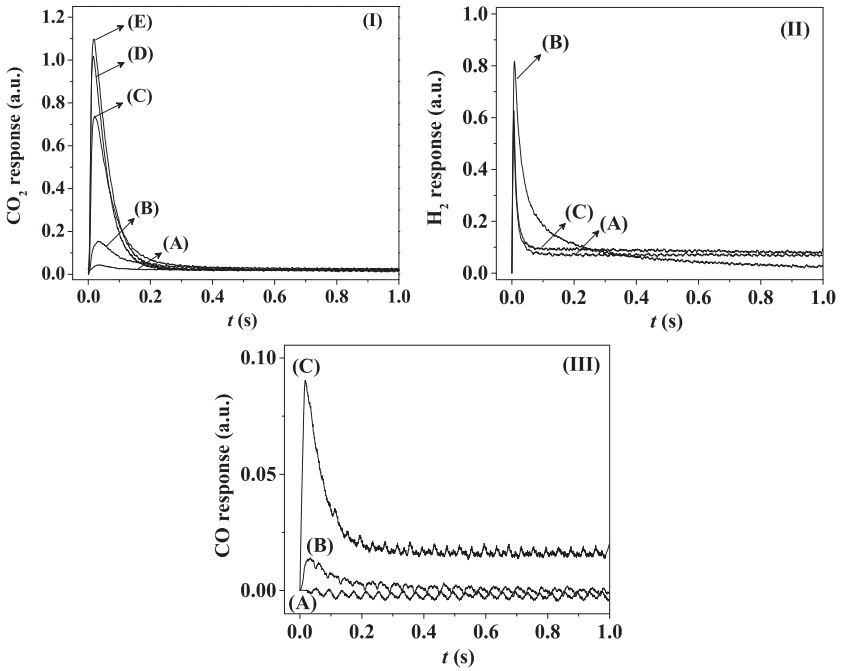

Fig. 7. The response of **(I)** CO_2, **(II)** H_2 and **(III)** CO in the pulse reaction over **(A)** Ni/CeO_2, **(B)** Ni/TiO_2, **(C)** Ni/SiO_2; **(ID)** CO_2 signal over CeO_2 and **(IE)** CO_2 signal in blank test.

3.3. Tuning metal-oxide interaction

Reduction temperature impacts on metal particle morphology, support surface properties and the metal-support interaction, which in turn influences reactant adsorption/activation [54,55]. Ni particle morphology and metal-support interaction of Ni/CeO_2 (activated at 773 K and 973 K) was examined by HRTEM with representative images presented in Fig. 8 and **Fig. S2**. The image of Ni/CeO_2 activated at 773 K presented Ni nanoparticles with size (3–22 nm, mean = 8.7 nm, **Fig. S2A**). Clear interface boundary between Ni and CeO_2 was observed (dashed frame, **(A)**). In contrast to the catalyst activated at 723 K, reduction at higher temperature (773 K) induced decoration of Ni nanoparticles due to migration of reduced ceria to Ni nanocrystallites. A further increase in reduction temperature (to 973 K) resulted in formation of quasi-spherical Ni nanoparticles. There was no significant change of Ni particle size (3–21 nm, mean = 9.4 nm, **Fig. S2B**), in agreement with the consensus that surface oxygen vacancies served to anchor/stabilise Ni nanoparticles [25]. Activation of Ni/CeO_2 at 973 K (**B**) caused encapsulation of Ni nanoparticles by ceria with a higher coverage (> 70%) of Ni surface.

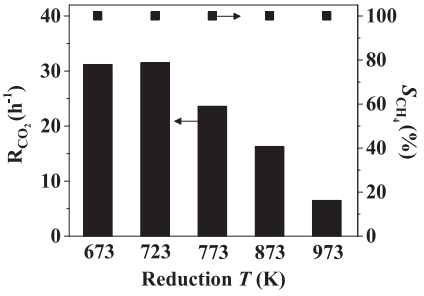

Fig. 9. Effect of reduction temperature (673–973 K) on CO_2 consumption rate (R_{CO_2}) in CO_2 methanation over Ni/CeO_2. Reaction condition: T_{react} = 523 K, $n/F_{CO_2} = 6.5 \times 10^{-3}$ h, GHSV = 6.6×10^4 h^{-1}.

The effect of reduction temperature on the catalytic response in CO_2 methanation (523 K) over Ni/CeO_2 was presented in Fig. 9. Methane was the sole product under the investigated reduction temperature range (673–973 K). The CO_2 consumption rate was kept constant with increasing reduction temperature from 673 K to 723 K A further

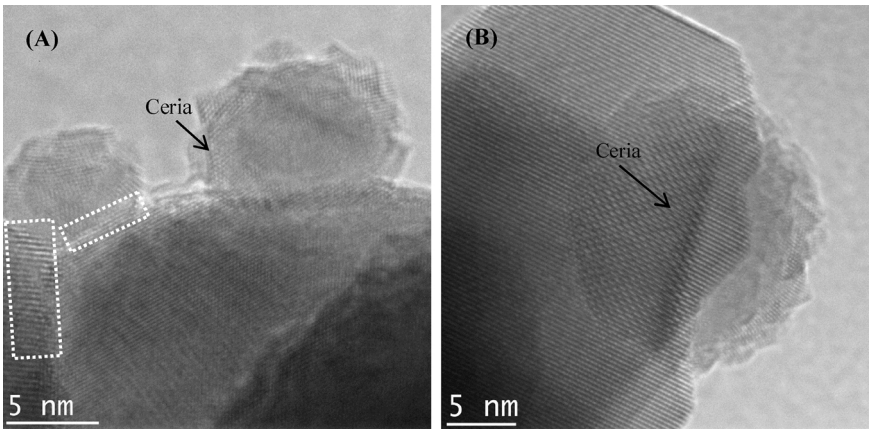

Fig. 8. Representative HRTEM images for Ni/CeO_2 reduced at **(A)** 773 K and **(B)** 973 K.

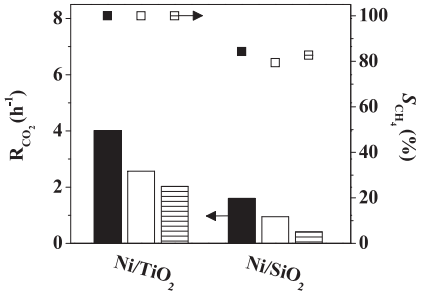

Fig. 10. Variation of CO_2 consumption rate (R_{CO_2}) and CH_4 selectivity (S_{CH_4}) with reduction temperature (solid bar: 723 K, open bar: 773 K, line bar: 973 K) in CO_2 methanation over (TiO_2 and SiO_2) supported Ni catalyst. Reaction condition: T_{react} = 523 K, n/F_{CO_2} = 6.5×10^{-3}-2.6×10^{-2} h, GHSV = 1.6×10^4-6.6×10^4 h^{-1}.

increase in reduction temperature (723 K → 973 K) resulted in lower CO_2 consumption rate. This suggests decoration/encapsulation of Ni particles do not favour activation of CO_2 and/or H_2 for reaction. This is consistent with the published study which has shown that high extent of encapsulation of Ru particles by TiO_x sublayer largely decreased the CO_2 methanation rate [56]. Moreover, Rodriguez et al. [6] reported that complete surface coverage of Cu (111) by reduced ceria did not show any activity in the CO_2 hydrogenation to methanol. We consider higher coverage of Ni surface by reduced ceria layer due to decoration/encapsulation effect must decrease the interface boundary perimeter and exposed Ni surface, which consequently lowered catalytic capacity of Ni/CeO_2 for activation of CO_2 and/or H_2. For a comparison, (TiO_2 and SiO_2) supported Ni catalysts were reduced at 723–973 K and tested in CO_2 methanation. The CO_2 conversion rate was decreased with increasing reduction temperature (Fig. 10). TEM images of Ni/TiO_2 activated at 973 K as a representative are shown in **Fig. S3**. Appreciably larger Ni particles (mean = 24.8 nm) due to agglomeration of Ni particles were observed post-reduction at 973 K relative to that (mean = 9.4 nm) at 723 K. The decreased activity at higher reduction temperature for reaction over Ni/TiO_2 and Ni/SiO_2 can be linked to large Ni particle sizes that decreased active surface area for CO_2 and/or H_2 activation. CH_4 selectivity was similar to that observed in Fig. 6. We can note that Ni/CeO_2 still exhibited higher methanation rates than that recorded over (TiO_2 and SiO_2) supported Ni catalysts, suggesting the metal-oxide interfacial effect favoured CO_2 methanation.

3.4. Catalytic stability

The long-term catalytic stability of Ni/CeO_2 was examined in CO_2 methanation (523 K); the time on-stream conversion and CH_4 selectivity profile is presented in Fig. 11. CO_2 was exclusively converted to CH_4 within 50 h. An initial loss of activity was observed with steady state attained after 10 h on-stream. The catalyst degradation in CO_2 methanation has been linked to Ni sintering and carbon deposition

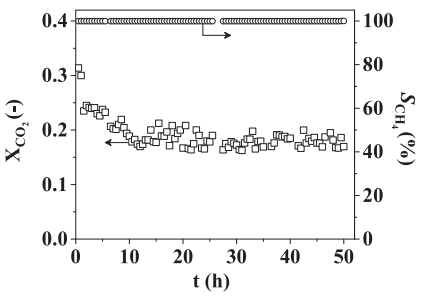

Fig. 11. Catalytic stability of Ni/CeO_2 in CO_2 methanation. Reaction condition: T_{react} = 523 K, T_{reduce} = 723 K, n/F_{CO_2} = 6.5×10^{-3} h, GHSV = 6.6×10^4 h^{-1}.

[28,57]. The spent catalyst was subjected to BET, TEM, XRD and TG-DTG to study the catalyst deactivation. The spent Ni/CeO_2 showed a SSA (10 $m^2 g^{-1}$), close to that (11 $m^2 g^{-1}$) recorded over the catalyst pre-reaction. HRTEM analysis (Fig. 12**(I)**) revealed a change in Ni particle morphology to the quasi-spherical shape post-reaction from the hexagonal crystallites pre-reaction, suggesting a reconstruction of Ni surface occurred during reaction. The histogram of Ni nanoparticle size for the spent Ni/CeO_2 catalyst (**II**) showed a wider size range (4–17 nm) with a larger mean (9.5 nm) relative to that (3–14 nm, 8.7 nm) recorded over the sample pre-reaction, indicating agglomeration and sintering of Ni particles to some extent. No carbon whisker was observed on the catalyst surface. Czekaj et al. [58] have reported whisker carbon formation on Ni particles in the methanation of syngas over Ni/Al_2O_3 at high temperature (≥673 K). This suggests whisker carbon formation was thermodynamically suppressed under the reaction condition (523 K) employed in this study. XRD analysis (using Cu radiation) for the spent Ni/CeO_2 **(III)** revealed phases of metallic Ni and cubic ceria. There was no detectable signal due to crystalline carbon (graphite and whisker carbon) and NiO. To further probe the possible formation of carbon, TG-DTG analysis for Ni/CeO_2 pre- and post-reaction was conducted with results shown in Fig. 12**(IV)**. Pre-reaction, the activated Ni/CeO_2 exhibited weight loss (0.35%) at T ≤ 463 K due to water removal and mass increase at higher temperature (463–773 K) that can be attributed to oxidation of metallic Ni to NiO and/or support ceria (Ce^{3+} → Ce^{4+}). TG analysis of the spent Ni/CeO_2 generated a signal response similar to that of the activated sample. The mass loss (0.40%) below 483 K can be attributed to water removal and/or desorption of adsorbed reactants/products (e.g., CO_2, H_2 and CH_4). The weight increase within 483–683 K was lower (by 0.15%) than that recorded over the activated Ni/CeO_2. There was no change in weight above 773 K, indicating no whisker carbon formation [59]. DTG analysis generated profiles for Ni/CeO_2 pre- and post-reaction overlapped with each other. The change in weight did not vary with temperature, confirming there was no carbon deposit on catalyst surface post-reaction. Based on the characterisation results, the initial loss of activity can be principally attributed to a reconstruction of Ni nanoparticles to quasi-spherical morphology from hexagonal crystallites.

4. Conclusion

We have presented metal-support interaction governs CO_2 activation/conversion for methane production over (CeO_2, TiO_2 and SiO_2) supported Ni nanoparticles. HRTEM analysis of Ni/CeO_2 (activated at 723 K) presented hexagonal Ni nanocrystallites, defects and strong interaction between Ni and CeO_2. While TiO_2 and SiO_2 as supports favoured formation of pseudo-spherical Ni nanoparticles. TPR, XPS and UV Raman analysis for Ni/CeO_2 revealed partial reduction of ceria surface with generation of oxygen vacancies. Reaction over Ni/CeO_2 delivered full selectivity to CH_4 with (up to forty-fold) higher TOF than that recorded over (TiO_2 and SiO_2) supported Ni nanoparticles. Ni/SiO_2 promoted CO formation as by-product. Pulse reaction by TAP demonstrated a stronger adsorption of CO_2 and H_2 on Ni/CeO_2. Activation of Ni/CeO_2 at higher temperature (773–973 K) resulted in decoration/encapsulation of Ni nanoparticles by ceria layer, which lowered CO_2 conversion to CH_4. An initial loss of activity in the catalytic stability evaluation can be principally linked to a reconstruction of Ni surface.

Acknowledgements

This work was financially supported by European Commission 7th Framework Programme: BIOGO-for-Production (Grant No. 604296). We thank Mr. Lucas Tillman, Prof. Shanwen Tao and Dr. Marc Walker for their contribution to this work.

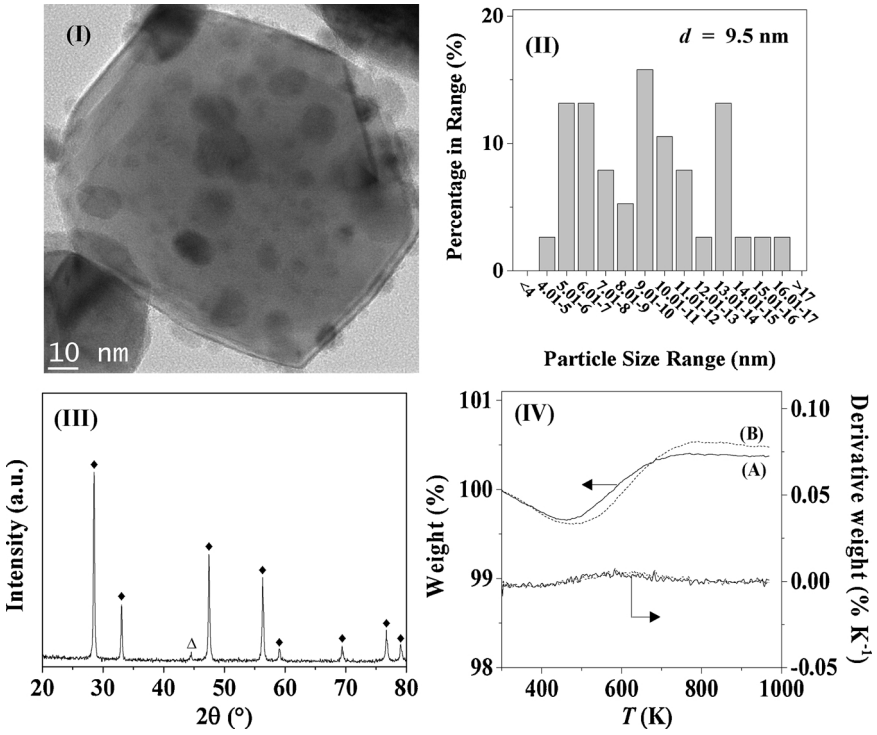

Fig. 12. **(I)** Representative HRTEM image, **(II)** associated histogram of Ni particle size distribution, **(III)** XRD pattern for Ni/CeO_2 post-reaction (Δ: Ni; ♦: CeO_2) and **(IV)** TG-DTG profile of the **(A)** activated and **(B)** spent Ni/CeO_2.

Appendix A. Supplementary data

Supplementary material related to this article can be found, in the online version, at doi:https://doi.org/10.1016/j.apcatb.2018.07.074.

References

[1] P.C. Stair, Nat. Chem. 3 (2011) 345–346.
[2] B.D. Chandler, Nat. Chem. 9 (2017) 108–109.
[3] J.Y. Park, L.R. Baker, G.A. Somorjai, Chem. Rev. 115 (2015) 2781–2817.
[4] M. Cargnello, V.V.T. Doan-Nguyen, T.R. Gordon, R.E. Diaz, E.A. Stach, R.J. Gorte, P. Fornasiero, C.B. Murray, Science 341 (2013) 771–773.
[5] R.F. Klie, M.M. Disko, N.D. Browning, J. Catal. 205 (2002) 1–6.
[6] J.A. Rodriguez, D.C. Grinter, Z.Y. Liu, R.M. Palomino, S.D. Senanayake, Chem. Soc. Rev. 46 (2017) 1824–1841.
[7] K. Cheng, N.N. Han, Y. Su, J.F. Zhang, J.J. Zhao, Sci. Rep. 7 (2017) 41771.
[8] K. Larmier, W.C. Liao, S. Tada, E. Lam, R. Verel, A. Bansode, A. Urakawa, A. Comas-Vives, C. Coperet, Angew. Chem. Int. Ed. 56 (2017) 2318–2323.
[9] A. Picone, M. Riva, A. Brambilla, A. Calloni, G. Bussetti, M. Finazzi, F. Ciccacci, L. Duo, Surf. Sci. Rep. 71 (2016) 32–76.
[10] K. Qadir, B.T.P. Quynh, H. Lee, S.Y. Moon, S.H. Kim, J.Y. Park, Chem. Commun. 51 (2015) 9620–9623.
[11] J.A. Rodriguez, P. Liu, D.J. Stacchiola, S.D. Senanayake, M.G. White, J.G.G. Chen, ACS Catal. 5 (2015) 6696–6706.
[12] S.D. Senanayake, P.J. Ramirez, I. Waluyo, S. Kundu, K. Mudiyanselage, Z.Y. Liu, Z. Liu, S. Axnanda, D.J. Stacchiola, J. Evans, J.A. Rodriguez, J. Phys. Chem. C 120 (2016) 1778–1784.
[13] J.C. Matsubu, S.Y. Zhang, L. De Rita, N.S. Marinkovic, J.G.G. Chen, G.W. Graham, X.Q. Pan, P. Christopher, Nat. Chem. 9 (2017) 120–127.
[14] S. Bernal, F.J. Botana, J.J. Calvino, C. López, J.A. Pérez-Omil, J.M. Rodríguez-Izquierdo, J. Chem. Soc. Faraday Trans. 92 (1996) 2799–2809.
[15] A. Berko, N. Balazs, G. Kassab, L. Ovari, J. Catal. 289 (2012) 179–189.
[16] Z. Majzik, N. Balazs, A. Berko, J. Phys. Chem. C 115 (2011) 9535–9544.
[17] S. Bernal, J.J. Calvino, M.A. Cauqui, J.M. Gatica, C.L. Cartes, J.A.P. Omil, J.M. Pintado, Catal. Today 77 (2003) 385–406.
[18] T. Komaya, A.T. Bell, Z. Wengsieh, R. Gronsky, F. Engelke, T.S. King, M. Pruski, J. Catal. 149 (1994) 142–148.
[19] Z.H. Qin, M. Lewandowski, Y.N. Sun, S. Shaikhutdinov, H.J. Freund, J. Phys. Chem. C 112 (2008) 10209–10213.
[20] M.G. Willinger, W. Zhang, O. Bondarchuk, S. Shaikhutdinov, H.J. Freund, R. Schlogl, Angew. Chem. Int. Ed. 53 (2014) 5998–6001.
[21] S. Bonanni, K. Ait-Mansour, H. Brune, W. Harbich, ACS Catal. 1 (2011) 385–389.
[22] H.L. Tang, J.K. Wei, F. Liu, B.T. Qiao, X.L. Pan, L. Li, J.Y. Liu, J.H. Wang, T. Zhang, J. Am. Chem. Soc. 138 (2016) 56–59.
[23] X.Y. Liu, M.H. Liu, Y.C. Luo, C.Y. Mou, S.D. Lin, H.K. Cheng, J.M. Chen, J.F. Lee, T.S. Lin, J. Am. Chem. Soc. 134 (2012) 10251–10258.
[24] D.F. Gao, Y. Zhang, Z.W. Zhou, F. Cai, X.F. Zhao, W.G. Huang, Y.S. Li, J.F. Zhu, P. Liu, F. Yang, G.X. Wang, X.H. Bao, J. Am. Chem. Soc. 139 (2017) 5652–5655.
[25] C.T. Campbell, C.H.F. Peden, Science 309 (2005) 713–714.
[26] W.H. Bernskoetter, N. Hazari, Acc. Chem. Res. 50 (2017) 1049–1058.
[27] H. Muroyama, Y. Tsuda, T. Asakoshi, H. Masitah, T. Okanishi, T. Matsui, K. Eguchi, J. Catal. 343 (2016) 178–184.
[28] A. Vita, C. Italiano, L. Pino, P. Frontera, M. Ferraro, V. Antonucci, Appl. Catal. B: Environ. 226 (2018) 384–395.
[29] C. Mebrahtu, S. Abate, S. Perathoner, S. Chen, G. Centi, Catal. Today 304 (2018) 181–189.
[30] J. Wei, Q.J. Ge, R.W. Yao, Z.Y. Wen, C.Y. Fang, L.S. Guo, H.Y. Xu, J. Sun, Nat. Commun. 8 (2017) 15174–15182.
[31] S.Y. Xiao, Z.Y.J. Meng, Chem. Soc. Faraday Trans. 90 (1994) 2591–2595.
[32] A.C. van Veen, O. Hinrichsen, M. Muhler, J. Catal. 210 (2002) 53–66.
[33] N. Laosiripojana, S. Assabumrungrat, S. Charojrochkul, Appl. Catal. A Gen. 327 (2007) 180–188.
[34] J.X. Guo, J. Liang, Y.H. Chu, M.C. Sun, H.Q. Yin, J.J. Li, Appl. Catal. A Gen. 421 (2012) 142–147.
[35] M.S. Li, X.D. Wang, F. Cárdenas-Lizana, M.A. Keane, Catal. Today 279 (2017) 19–28.
[36] A. Vita, C. Italiano, C. Fabiano, M. Lagana, L. Pino, Mater. Chem. Phys. 163 (2015) 337–347.
[37] S. Mahammadunnisa, P.M.K. Reddy, N. Lingaiah, C. Subrahmanyam, Catal. Sci. Technol. 3 (2013) 730–736.
[38] P. Lakshmanan, M.S. Kim, E.D. Park, Appl. Catal. A Gen. 513 (2016) 98–105.
[39] X. Chen, M. Li, J.C. Guan, X.K. Wang, C.T. Williams, C.H. Liang, Ind. Eng. Chem. Res. 51 (2012) 3604–3611.
[40] V.M. Shinde, G. Madras, RSC Adv. 4 (2014) 4817–4826.
[41] M.C. Biesinger, B.P. Payne, A.P. Grosvenor, L.W.M. Lau, A.R. Gerson, R.S. Smart, Appl. Surf. Sci. 257 (2011) 2717–2730.
[42] M. Baron, O. Bondarchuk, D. Stacchiola, S. Shaikhutdinov, H.J. Freund, J. Phys. Chem. C 113 (2009) 6042–6049.
[43] E. Beche, P. Charvin, D. Perarnau, S. Abanades, G. Flamant, Surf. Interface Anal. 40 (2008) 264–267.
[44] M.V. Ganduglia-Pirovano, A. Hofmann, J. Sauer, Surf. Sci. Rep. 62 (2007) 219–270.
[45] A. Trovarelli, C. Deleitenburg, G. Dolcetti, J.L. Lorca, J. Catal. 151 (1995) 111–124.
[46] C. Ao, P.F. Tian, L.K. Ouyang, G.J. Da, X.Y. Xu, J. Xu, Y.F. Han, Catal. Sci. Technol. 6 (2016) 5060–5068.
[47] M. Guo, J.Q. Lu, Y.N. Wu, Y.J. Wang, M.F. Luo, Langmuir 27 (2011) 3872–3877.
[48] T. Taniguchi, T. Watanebe, S. Ichinohe, M. Yoshimura, K. Katsumata, K. Okada, N. Matsushita, Nanoscale 2 (2010) 1426–1428.
[49] N. Wang, W.Z. Qian, W. Chu, F. Wei, Catal. Sci. Technol. 6 (2016) 3594–3605.
[50] W.L. Zhen, F. Gao, B. Tian, P. Ding, Y.B. Deng, Z. Li, H.B. Gao, G.X. Lu, J. Catal. 348 (2017) 200–211.
[51] P. Panagiotopoulou, Appl. Catal. A Gen. 542 (2017) 63–70.
[52] S.W. Cao, F. Tao, Y. Tang, Y.T. Li, J.G. Yu, Chem. Soc. Rev. 45 (2016) 4747–4765.

[53] Y.N. Xia, Y.J. Xiong, B. Lim, S.E. Skrabalak, Angew. Chem. Int. Ed. 48 (2009) 60–103.
[54] S. Tada, R. Kikuchi, K. Urasaki, S. Satokawa, Appl. Catal. A Gen. 404 (2011) 149–154.
[55] V.P. Londhe, V.S. Kamble, N.M. Gupta, J. Mol. Catal. A: Chem. 121 (1997) 33–44.
[56] J.H. Xu, X. Su, H.M. Duan, B.L. Hou, Q.Q. Lin, X.Y. Liu, X.L. Pan, G.X. Pei, H.R. Geng, Y.Q. Huang, T. Zhang, J. Catal. 333 (2016) 227–237.
[57] B. Miao, S.S.K. Ma, X. Wang, H.B. Su, S.H. Chan, Catal. Sci. Technol. 6 (2016) 4048–4058.
[58] I. Czekaj, F. Loviat, F. Raimondi, J. Wambach, S. Biollaz, A. Wokaun, Appl. Catal. A Gen. 329 (2007) 68–78.
[59] E.H. Yang, D.J. Moon, RSC Adv. 6 (2016) 112885–112898.